confirm that reoxidation of a similarly reduced catalyst yielded α_I-$VOPO_4$.

We validated the self-modeling analysis with two methods: (i) Comparison of the positions of the pre-edge feature and the main absorption edge in each of the spectra generated from the self-modeling analysis with the values of those features measured for a series of vanadium oxide reference materials (*23*); and (ii) Comparison of the self-modeling composition profiles to those generated by modeling the data as a set of Lorentzians. As evident in Fig. 3, A and B, the position of the pre-edge and edge features correlated well with those collected from the reference materials. In Fig. 2A, we present the composition profiles determined for reaction at 320°C by modeling the data as a set of Lorentzians. The Lorentzian analysis and the factor analysis agree quite well. However, unlike the more traditional curve fitting, self-modeling analysis does not require reference compounds (that is, they are extracted from the data self-consistently), and the large amount of data collected in a transient dispersive XAS experiment can be handled easily.

To confirm that the above results relate to the $(VO)_2P_2O_7$ phase, we conducted similar experiments on the $(VO)_2P_2O_7/SiO_2$ catalyst. The results obtained for reduction at 380°C in 10% C_4H_{10}/Ar are shown in Fig. 4. The profile for the decay of the V^{5+} concentration matches well that for production of maleic anhydride, with the reaction to more completely oxidized products easily accounting for the mismatch observed at longer times.

REFERENCES AND NOTES

1. T. R. Felthouse, J. C. Burnett, S. F. Mitchell, M. J. Mummy, *Kirk-Othmer Encyclopedia of Chemical Technology* (Wiley, New York, 1995), pp. 893–928.
2. P. Mars and D. W. v. Krevelen, *Chem. Eng. Sci.* **3**, 41 (1954).
3. S. K. Bej and M. S. Rao, *Ind. Eng. Chem. Res.* **31**, 2075 (1992).
4. F. Trifiro, *Catal. Today* **16**, 91 (1993).
5. M. Misono *et al.*, in *New Developments in Selective Oxidation*, G. Centi and F. Trifiro, Eds. (Elsevier, Amsterdam, 1990), p. 605.
6. B. Schiott and K. A. Jorgensen, *Catal. Today* **16**, 79 (1993).
7. G. Centi, *ibid.*, p. 5.
8. G. J. Hutchings, A. Desmartin-Chomel, R. Olier, J. C. Volta, *Nature* **368**, 41 (1994).
9. A. Soejarto, G. Schrader, G. S. Coulston, *Can. J. Chem. Eng.*, in press.
10. E. Bordes, *Catal. Today* **16**, 27 (1993).
11. B. K. Hodnett, *ibid.*, p. 131.
12. J. T. Ebner and M. R. Thompson, *ibid.*, p. 51.
13. P. L. Gai and K. Kourtakis, *Science* **267**, 661 (1995).
14. K. Tamaru, in *Catalysis: Science and Technology*, J. R. Anderson and M. Boudart, Eds. (Springer-Verlag, Berlin, 1991), pp. 87–129.
15. The α_I-$VOPO_4/SiO_2$ catalyst was prepared by wet impregnation. Davisil silica (grade 644) was washed in 1 M nitric acid at 80°C for 48 hours and then rinsed repeatedly with doubly deionized water until the washings tested pH neutral. Air calcination at 90°C overnight, and subsequently at 520°C for 6 hours, removed labile hydroxyls and surface nitrates. The resulting silica had a surface area of 338 m^2/g determined by the Brunauer-Emmett-Teller (BET) N_2 adsorption method. The silica was impregnated under conditions of incipient wetness with an aqueous solution containing ammonium metavanadate, oxalic acid, and dibasic ammonium phosphate. The solution concentrations were adjusted to obtain an elemental P:V ratio of 1:1 and a 6 weight % vanadium loading on the silica support. The P:V ratios and loading were confirmed with inductively coupled plasma-optical emission spectroscopy (ICP), and the crystalline phase was confirmed by x-ray diffraction and laser Raman spectroscopy (514 nm). The impregnated silica was dried in air at 90°C overnight at 200°C for 2 hours, and finally at 500°C for 6 hours. The resulting material had a 181-m^2/g surface area. The $(VO)_2P_2O_7/SiO_2$ catalyst was prepared as follows: 10.42 g of the cluster $[(VO)_4(P_2O_7)_2(CH_3O)_4]$ $(C_{14}H_{19}N_2)_4 \cdot (CH_3OH)_4$ (*16*) was dissolved into 50 ml of dry methanol in a glove box. The deep blue solution was impregnated into 10 g silica powder (BET surface area of 300 m^2/g), and the slurry was evaporated to dryness. The deep blue solid was calcined in flowing air to 350°C for 1 hour and recovered for use in TRXAS experiments. The x-ray absorption and reactivity measurements were performed with a Lytle-designed in situ cell (*17*). A catalyst sample was pressed into a self-supporting wafer ~150-μm thick to keep the vanadium absorbance ~1. A small amount of unpressed catalyst was placed in the reactor next to and upstream of the wafer to enhance the MS detection of product stream maleic anhydride. This configuration satisfied the Weisz-Prater criterion (*18*), which ensures that the wafer and unpressed catalyst exhibited identical kinetics. The experiments were performed at the NSLS X6A beamline at Brookhaven National Laboratory. The x-ray optics were configured as described elsewhere (*19*), with the exception that a bent Si(111) crystal was used to access energies at the vanadium K-edge (5.46 keV). The data were analyzed with a variant of self-modeling curve resolution (*20, 21*), the details of which will be published elsewhere (*22*). Briefly, the data matrix (**D**) was factored into two subspaces related to the spectral characteristics (**S**) and composition profiles (**C**), that is, **D** = **SC**. In our approach, an initial estimate for **C** was projected into the composition subspace of the data to generate a new approximation to **C** using **C** = **CUU**†, the constraint $C_{ij} > 0$ was applied, and iteration continued until the solution converged to a self-consistent set of concentration profiles and reference spectra. Singular value decomposition produced the matrix of significant right-hand eigenvectors **U**.
16. N. Herron, D. L. Thorn, R. L. Harlow, in preparation.
17. F. W. Lytle, The EXAFS Company, Pioche, NV 89043.
18. G. F. Froment and K. Bischoff, *Chemical Reactor Analysis and Design* (Wiley, New York, 1979).
19. P. L. Lee *et al.*, *Rev. Sci. Instrum.* **65**, 1 (1994).
20. E. R. Malinowski, *Factor Analysis in Chemistry* (Wiley, New York, 1991).
21. M. Fernandez-Garcia, C. M. Alvarez, G. L. Haller, *J. Phys. Chem.* **99**, 12565 (1995).
22. G. W. Coulston, in preparation.
23. J. Wong, F. W. Lytle, R. P. Messmer, D. H. Maylotte, *Phys. Rev. B* **30**, 5596 (1984).

24. We gratefully acknowledge the assistance of G. Jenning, who developed the beamline control software used in these experiments as well as J. Quintana for cutting the Si(111) crystal. This work was performed at the X6A beamline, National Synchrotron Light Source, Brookhaven National Laboratory, which is supported by the Divisions of Materials Science and Chemical Science of the U.S. Department of Energy. Work at Northwestern was supported by the Division of Chemical Sciences of DOE.

26 July 1996; accepted 17 October 1996

Crustal Deformation from 1992 to 1995 at the Mid-Atlantic Ridge, Southwest Iceland, Mapped by Satellite Radar Interferometry

Hélène Vadon and Freysteinn Sigmundsson

Satellite radar interferometry observations of the Reykjanes Peninsula oblique rift in southwest Iceland show that the Reykjanes central volcano subsided at an average rate of up to 13 millimeters per year from 1992 to 1995 in response to use of its geothermal field. Interferograms spanning up to 3.12 years also include signatures of plate spreading and indicate that the plate boundary is locked at a depth of about 5 kilometers. Below that depth, the plate movements are accommodated by continuous ductile deformation, which is not fully balanced by inflow of magma from depth, causing subsidence of the plate boundary of about 6.5 millimeters per year.

The mid-ocean rift system is subaerial in Iceland, and divergent plate motion across the North American–Eurasian plate boundary (Fig. 1, inset) can be observed there by geodetic measurements, which were first attempted in 1938 (*1*). Extensive projects of distance measurements and precise leveling were initiated in Iceland in the late 1960s (*2*), and in recent years Global Positioning System (GPS) geodesy has revolutionized crustal deformation monitoring in Iceland (*3*). An area of special interest is the 50 by 25 km Reykjanes Peninsula in southwest Iceland, as it is the direct onland structural continuation of the Mid-Atlantic Ridge. The Reykjanes Peninsula plate boundary is oriented at an oblique angle to the spreading direction, not at a right angle as are typical divergent plate boundaries. The full spreading vector there is 1.86 cm/year at N103°E (*4*), whereas the average direction of the plate boundary is ~N76°E. Predicted strike-slip and opening components across the boundary are accordingly 1.7 cm/year and 0.8 cm/year. Volcanic systems along

H. Vadon, Centre National d'Études Spatiales, 18 Avenue Edouard Belin, 31055, Toulouse, France.
F. Sigmundsson, Nordic Volcanological Institute, University of Iceland, Grensasvegur 50, IS-108 Reykjavik, Iceland.

the plate boundary consist of a central volcano, where volcanic production is highest and high-temperature geothermal areas are located, and a transecting fissure swarm (Fig. 1) (5). Earthquakes occur mainly at depths of 1 to 5 km, in a zone 2 to 5 km wide that marks the central axis of the plate boundary (6). One magnitude 6 (M 6) earthquake and several M 4 to 5 earthquake swarms occurred on the peninsula from 1967 to 1975, but since then seismic activity has been low.

Plate movements cause continuous crustal deformation within plate boundary zones (7). Within these zones, there is a spatially varying crustal velocity field (8), whereas plate interiors move more like rigid units. The data we present put constraints on the crustal velocity field at the Reykjanes Peninsula, as well as on deformation of the Reykjanes central volcano. Previous geodetic work in the area includes GPS measurements at seven sites from 1986 to 1992 (9), confirming left-lateral shear accumulation across the peninsula and suggesting a plate boundary locking depth between 5 and 11 km. Subsidence at the Reykjanes central volcano where geothermal exploitation takes place has been documented by extensive geodetic leveling in the period from 1975 to 1992 (*10*), and more limited leveling data at other parts of the peninsula suggest continuous long-term subsidence along the whole plate boundary (*11*). Our observations provide unprecedented spatial resolution and coverage of the combined deformation indicated by the above-mentioned data.

Satellite-based synthetic aperture radar (SAR) interferometry has proved its ability to build images of ground surface deformation, an ability that is usable in a wide range of applications (*12*). We used the technique to form interferograms covering our study area, using radar images from the European Space Agency Remote Sensing Satellite (ERS-1) (*13*). After correction for known topographic and orbital effects, the interferograms include information about the ground-to-satellite component of crustal motion but may also contain noise caused by the atmosphere, by changes in surface backscattering characteristics, and by in-

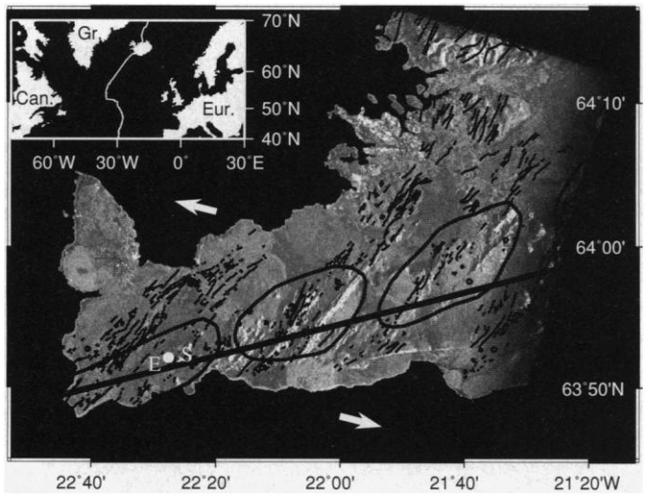

Fig. 1. Radar amplitude image of the Reykjanes Peninsula in southwest Iceland. Added to the image are faults and eruptive fissures and the outlines of central volcanoes (circled areas). The thick line indicates the approximate location of the central axis of the plate boundary as inferred from seismicity. The Reykjanes central volcano is farthest to the west; there we find a center of subsidence (circle) close to the Svartsengi (S) and Eldvorp (E) geothermal fields. Arrows indicate the direction of plate motion. The small inset (with land in white and sea in black) shows the location of Iceland in the North Atlantic. Gr., Greenland; Can., Canada; Eur., Europe. The white line represents the Mid-Atlantic Ridge, which is submarine except in Iceland.

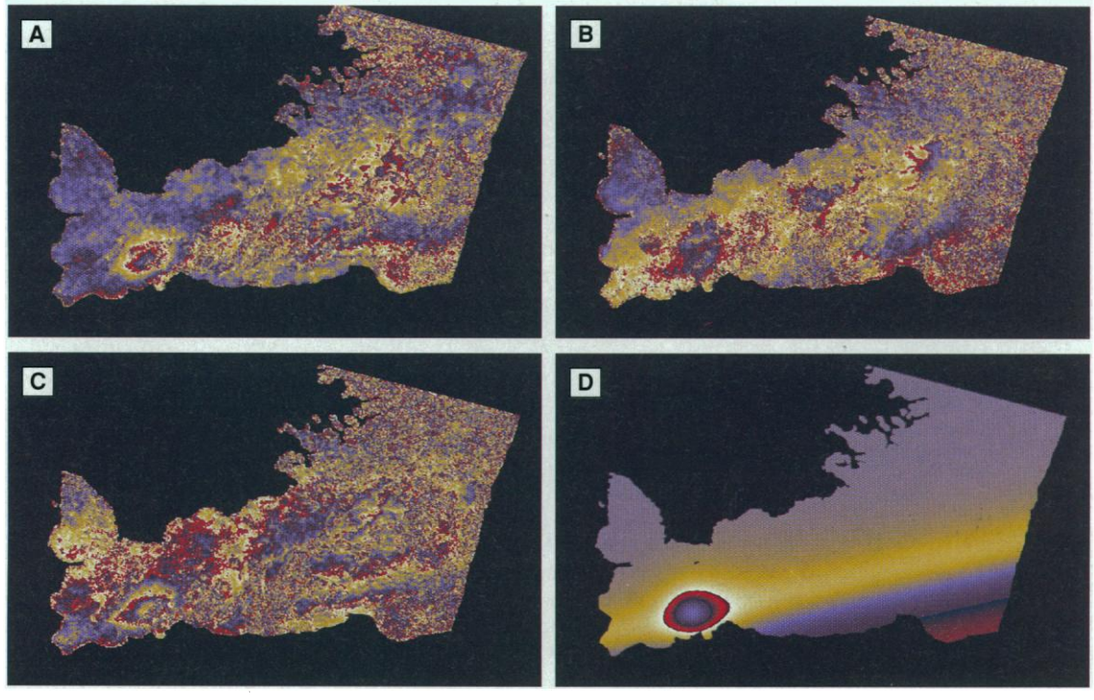

Fig. 2. Interferograms covering 0.83 years (**A**), 2.29 years (**B**), and 3.12 years (**C**), and model interferogram showing best-fit simulated 2.29-year deformation (**D**). Time-progressive fringes appearing consistently in the interferograms are indicative of crustal deformation. Phases coded into bytes (8 bits) are represented here with a false color table. A complete color cycle, for example from blue to blue, represents one complete fringe; a 28-mm change in range in the case of ERS. Concentric fringes at the Reykjanes central volcano (Fig. 1) manifest a time-progressive increase in range to the satellite. The change in range is largest in the 3.12-year interferogram (C), where it is ~1.5 fringes (Fig. 3). An increase in range along the whole plate boundary, indicative of spreading, is visible as a central fringe in the 2.29-year (B) and 3.12-year (C) interferograms. The signal decreases in the eastern part of both interferograms [the end of the yellow color in (B) and the closed fringe in (C)]. This is probably a result of change in the plate boundary direction in this area, in which the direction becomes more aligned in the direction of plate movements (not accounted for in our modeling). Opening across the plate boundary is then less, and less subsidence is expected. Increasing the complexity of our model could result in a better fit but is not justified by the present data.

complete topographic and orbital corrections (*14*).

Initially, two images acquired during a descending satellite pass in the summer of 1992 were available. We selected the best matching summer images for 1993 and 1995. No suitable image was available for summer 1994, because the ERS-1 orbital cycle was different then. We determined the best images by evaluating the "altitude of ambiguity" of all available image pairs. The altitude of ambiguity is the ground altitude difference that generates one fringe in an interferogram (*15*). The higher the altitude of ambiguity, the fewer residual topographic fringes in the interferogram. We processed four images and from these we formed six interferograms (Table 1) covering periods from 35 days to 3.22 years. Some of the interferograms contained remaining orbital fringes that were due to inaccurate data on satellite position and were recognizable as a few parallel fringes regularly spaced over the whole interferogram. Those fringes were easily suppressed by subtraction of the corresponding phase gradient. Among the six interferograms produced, we used the 0.83-, 2.29-, and 3.12-year ones for modeling (Fig. 2, A through C). We used a digital elevation model (DEM) from the Icelandic Geodetic Survey, with a grid interval of 3″ in latitude (92 m) and 6″ in longitude (81 m). Our interferograms are in the DEM geometry—each interferogram pixel represents the combination of all (~100) radar pixels within the respective DEM cell. The 35-day interferogram was not used for modeling because of its limited time span. However, it allowed us to verify that the DEM did not exhibit significant local errors because no visible residual topographic fringes were visible in it, although its altitude of ambiguity was lower than that of the interferograms we used in modeling. The two long-term interferograms based on orbit 5064 had low coherence (*16*) and we did not use them. Good coherence in some of our interferograms, despite snow cover during winter, shows that coherence is recovered after snow melt, at least on barren lava flows, which cover most of our study area.

Table 1. Characteristics of interferograms.

Master orbit	Date	Slave orbit	Date	Elapsed time (years)	Altitude of ambiguity (m)
5,064	04/07/92	5,565	08/08/92	35 days	−35.6
5,064	04/07/92	10,575	24/07/93	0.93	−25.1
5,064	04/07/92	21,941	25/09/95	3.22	−19.6
5,565	08/08/92	10,575	24/07/93	0.83	−59.0
5,565	08/08/92	21,941	25/09/95	3.12	−43.6
10,575	24/07/93	21,941	25/09/95	2.29	−166.0

The most obvious deformation signal in our interferograms is the presence of concentric fringes at the Reykjanes central volcano, which are indicative of subsidence (Figs. 2 and 3). The center of subsidence is located between the Svartsengi and Eldvorp geothermal fields (Fig. 1), but the common geothermal reservoir of these fields has been used by a geothermal power plant at Svartsengi. Geothermal power plants withdraw fluids and thereby lower pressure in subsurface geothermal reservoirs. This, in addition to drops in reservoir temperature, can cause subsidence (*17*). To mimic the observed deflation at Svartsengi, we used vertical and horizontal motion predicted by a simple model invoking a spherical source of varying pressure within an elastic half-space. This model is analogous to the "Mogi model" that is frequently applied to pressure changes in active volcano magma chambers but is applied here to compaction of a geothermal reservoir. The model has four parameters that can be expressed as the source latitude and longitude; its apparent centroid depth, d_{mogi}; and the maximum surface subsidence h_{mogi}, which occurs directly above the source (*18*).

Another signal in the interferograms is the presence of time-progressive fringes aligned in the NEE direction, which are best observed on the southeast part of the peninsula (Fig. 2). These are caused by crustal motion at the plate boundary. A horizontal velocity field consistent with the interferograms is

$$v_{horizontal} = v_{spreading}\,\pi^{-1}\arctan(y/d_{lock}) \quad (1)$$

where $v_{spreading}$ is the full spreading vector, y is the distance from the central axis of the plate boundary, and d_{lock} is its locking depth (*19*). The fringes indicate motion too large to be explained by horizontal movements only, therefore the rift zone has subsided. We include in our modeling subsidence caused by a line-source of pressure decrease within an elastic half-space (*20*). We fix its location below the central axis of the plate boundary, at its locking depth. Then

$$v_{vertical} = h_{rift}\,d_{lock}^{2}\,(d_{lock}^{2} + y^{2})^{-1} \quad (2)$$

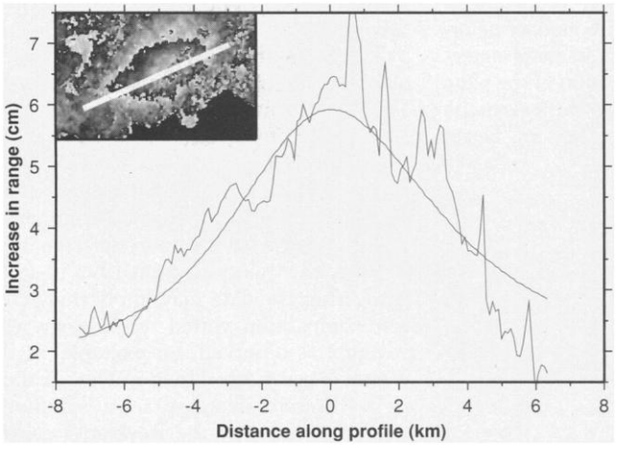

Fig. 3 (left). Change-in-range profile from 1992 to 1995 along the Reykjanes central volcano. Observed and modeled profiles are shown. The profile is almost parallel to the direction of the plate boundary. Changes are mostly due to the volcano pressure source. The inset shows part of Fig. 2C with the location of the profile.

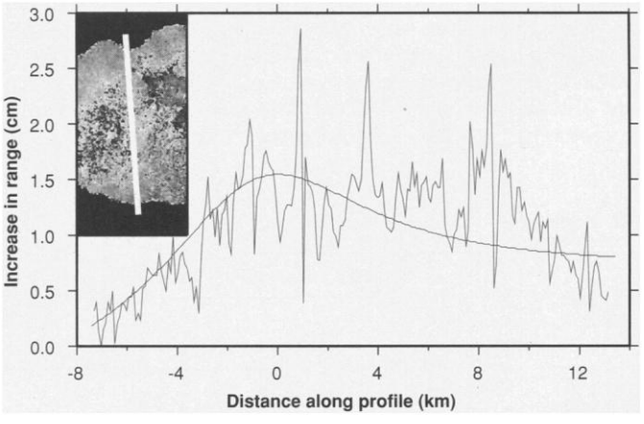

Fig. 4 (right). Change-in-range profile from 1993 to 1995 across the Reykjanes Peninsula, which is sufficiently far from the volcano pressure source that its effects are negligible. Changes are caused by plate movements. Observed and modeled profiles are shown. The inset shows part of Fig. 2B with the location of the profile.

where h_{rift} is the rate of subsidence along the central axis of the boundary. The line-source causes small horizontal contraction toward the plate boundary, resulting in a change in range of less than 1 mm/year that can be ignored.

When modeling the interferograms, we (i) calculated the expected three-dimensional deformation field, given initial values for the simulation parameters for a combined model of the volcano deflation and the rift deformation; (ii) projected the deformation vector onto the direction toward the satellite to derive the change in range; and (iii) generated a simulated fringe pattern from the predicted change in range. The unit vector in the direction from ground to satellite was (0.34, –0.095, 0.935) in the east, north, and vertical. The dominant contributor to the change in range is vertical deformation, because of the 23° ERS incidence angle. We tuned the model parameters to produce a simulated interferogram that best matched the observed one (Fig. 2D) by maximizing the global coherence of the residual interferograms (the difference between modeled and observed interferograms). To calculate global coherence, we considered phases as complex unitary numbers and summed all of them over the whole residual interferogram. The norm of this summed vector is a measure of how "flat" the interferogram is. The best global coherence gives the fewest remaining fringes and the most adequate model parameters. Quantifying the uncertainties is, however, complex, and we relied on visual inspection. We varied every parameter around its best-fit value and estimated visually when the residual interferogram degraded, indicating a lower fit.

A total of 11 scalar parameters are required in our simulation. The Mogi model has four parameters. Our model of plate boundary deformation based on Eqs. 1 and 2 requires three parameters that determine the location of the boundary central axis (latitude and longitude of a point on the axis and the axis direction) and the horizontal vector $v_{spreading}$, in addition to the d_{lock} and h_{rift} parameters. We did not estimate all of these parameters at the same time; we fixed the central axis of the plate boundary to its location inferred from seismicity (6) and $v_{spreading}$ to its predicted value (4). We initially estimated the latitude and longitude of the Mogi source, this location being at the center of the concentric fringes in the interferograms. Four parameters remained for each interferogram—d_{mogi}, h_{mogi}, d_{lock}, and h_{rift}—and we solved for these iteratively. The h_{mogi} parameter was the only one allowed to be time-dependent. We estimated the h_{mogi} parameter for the 3.12-year interferogram from a change-in-range profile across the subsidence area (Fig. 3). Other parameters were estimated with the use of the global coherence criteria. The overall increase in range at the plate boundary is best expressed in the 2.29-year interferogram (Fig. 2B), and we relied mainly on it when estimating the plate boundary parameters. The derived values are also adequate for the 3.12-year interferogram (Table 2).

The model interferograms replicate the features on the observed interferograms: both the concentric fringes at the Reykjanes central volcano and the regional NEE-directed fringes. Any model of a plate boundary with deformation varying with distance from its central axis will predict interferogram fringes that are aligned in the direction of the boundary. The predicted change in range, according to our plate boundary deformation model, is asymmetrical with respect to the central axis of the plate boundary (Fig. 4). Model interferogram fringes occur mainly at, and to the south of, the central axis (Fig. 2D) because of different contributions of horizontal and vertical deformation to the ground-to-satellite range change. The NEE-directed fringes we observe in the interferograms satisfy several criteria that justify our modeling of these as signatures of plate boundary deformation. Their direction is in good agreement with the average direction of the plate boundary as inferred from the seismicity and geodetic data (6, 9). They are better expressed in the SE part of the interferogram than elsewhere, and the global coherence of the residual interferograms is better if plate boundary deformation is considered than if it is ignored.

Seismicity (6) and horizontal displacements at seven sites in the area estimated from GPS measurements (9) indicated a plate boundary locking depth of 5 to 11 km, which is consistent with our determination of a locking depth of about 5 km. Our model predicts that 80% of the plate motion is accommodated within a zone only 30 km wide. The zone of active faulting and fissuring on the Reykjanes Peninsula has about this width, which is consistent with the narrow strain field indicated by our analysis. Our interpretation is that at a depth of about 5 km the deformation becomes mostly ductile and aseismic. A long-term subsidence along the whole plate boundary at a rate of about 6.5 mm/year, as we find, is also in agreement with repeated leveling on two profiles from 1966 to 1980 (*11*). These data suggest that the surface has tilted 0.5 to 1.0 μrad per year toward the central axis of the plate boundary. Our model is consistent with these values. A likely cause of subsidence along the plate boundary is loss of material below the locking depth. Extension within the ductile layer may be more local than in the elastic crust above, and flow of material from below is required to replace laterally displaced material. If this does not happen, the plate boundary subsides.

The subsidence of the Reykjanes central volcano from 1992 to 1995 is similar to subsidence observed there by leveling from 1975 to 1992 (*10*). Our inferred subsidence center lies between the Svartsengi and Eldvorp geothermal fields (Fig. 1). Several lines of evidence, such as good pressure connection between these areas, suggest that a common geothermal reservoir fuels both fields (*21*). Compaction of this reservoir caused by its use by the Svartsengi geothermal power plant can explain our observations to a large degree. The average rate of subsidence was up to 14 mm/year from 1975 to 1982 but decreased to 7 mm/year from 1985 to 1992. Then pressure in the reservoir apparently stabilized. Our data suggest that subsidence varied from 25 mm/year from 1992 to 1993, to 9 mm/year from 1993 to 1995. Altogether the data may imply that reservoir compaction varied nonlinearly with pressure, as observed, for example, at the Wairakei geothermal field in New Zealand (*17*). Pressure decrease in a solidifying magma chamber at the Reykjanes central volcano cannot be excluded as an alternate source of subsidence. Seismic waves passing beneath our inferred subsidence center at depths of 3 to 5 km show intense

Table 2. Modeling results. See text for discussion. Lat., latitude; Long., longitude.

Interferometric pair	Pressure source parameters				Rift parameters	
	h_{mogi} (mm)	d_{mogi} (km)	Lat.* (N°)	Long.* (W°)	h_{rift} (mm/year)	d_{lock} (km)
0.83 year, 1992–1993	21 ± 3					
2.29 year, 1993–1995	21 ± 3	4.6 ± 0.5	63.869	22.46	6.5 ± 1	5 ± 1.5
3.12 year, 1992–1995	42 ± 6					

*Estimated by visual inspection; 0.3 km uncertainty.

shear wave attenuation, and it has been inferred that a crustal magma chamber is present beneath this area (*22*), but this has not yet been confirmed. Our radar interferometry observations of deformation in southwest Iceland show that the technique can be used to monitor long-term strain buildup at plate boundaries and volcanoes and therefore may help to increase understanding of the preparatory processes of earthquakes and eruptions.

REFERENCES AND NOTES

1. In 1938, the first crustal deformation geodetic network was installed in Iceland, designed to detect extension across the North Iceland rift zone [O. Niemczyk, *Spalten auf Island* (Wittwer, Stuttgart, Germany, 1943)].
2. E. Tryggvason, *Cont. Oceanic Rifts Geodyn. Ser.* **8**, 17 (1982).
3. See, for example, G. R. Foulger *et al.*, *Nature* **358**, 488 (1992); F. Sigmundsson, P. Einarsson, R. Bilham, E. Sturkell, *J. Geophys. Res.* **100**, 6235 (1995).
4. According to the NUVEL-1A global plate motion model by C. DeMets, R. G. Gordon, D. F. Argus, and S. Stein [*Geophys. Res. Lett.* **21**, 2191 (1994)].
5. K. Saemundsson and S. Einarsson, *Geological Map of Iceland, Sheet 3, SW-Iceland, 2nd ed.* (Icelandic Museum of Natural History and Icelandic Geodetic Survey, Reykjavik, Iceland, 1980); P. Einarsson and K. Saemundsson, accompanying map in *I Hlutarins Edli*, T. Sigfusson, Ed. (Menningarsjodur, Reykjavik, Iceland, 1987).
6. P. Einarsson, *Tectonophysics* **189**, 261 (1991); F. W. Klein, P. Einarsson, M. Wyss, *J. Geophys. Res.* **78**, 5084 (1973); *ibid.* **82**, 865 (1977); P. Halldorsson, R. Stefansson, P. Einarsson, S. Bjornsson, *Estimate of Earthquake Risk* (Ministry of Industry, Reykjavik, Iceland, 1984).
7. R. G. Gordon and S. Stein, *Science* **256**, 333 (1992).
8. M. Lisowski, J. C. Savage, W. H. Prescott, *J. Geophys. Res.* **96**, 8369 (1991).
9. E. Sturkell, F. Sigmundsson, P. Einarsson, R. Bilham, *Geophys. Res. Lett.* **21**, 125 (1994).
10. H. Eysteinsson, *Leveling and Gravity Measurements in the Outer Part of the Reykjanes Peninsula 1992* (Report OS-93029, National Energy Authority, Reykjavik, Iceland, 1993).
11. E. Tryggvason, in *Geodynamics of Iceland and the North Atlantic Area*, L. Kristjánsson, Ed. (Reidel, Dordrecht, Netherlands, 1974), pp. 241–262; E. Tryggvason, *Vertical Component of Ground Deformation in Southwest and North Iceland* (Report 8102, Nordic Volcanological Institute, Reykjavik, Iceland, 1981).
12. D. Massonnet *et al.*, *Nature* **364**, 138 (1993); D. Massonnet, K. Feigl, M. Rossi, F. Adragna, *ibid.* **369**, 227 (1994); D. Massonnet, W. Thatcher, H. Vadon, *ibid.* **382**, 612 (1996); D. Massonnet, P. Briole, A. Arnaud, *ibid.* **375**, 567 (1995); R. M. Goldstein, H. Engelhardt, B. Kamb, R. M. Frolich, *Science* **262**, 1525 (1993).
13. The ERS-1 and ERS-2 satellites have sun-synchronous near polar orbits, with a mean altitude of 785 km and an inclination of 98.5°. The orbital cycle is 35 days in normal operational phase. Onboard SAR instruments operate in the C band, with a wavelength of 5.656 cm.
14. D. Massonnet and K. Feigl, *Geophys. Res. Lett.* **22**, 1537 (1995).
15. D. Massonnet, H. Vadon, M. Rossi, *IEEE Trans. Geosci. Remote Sens.* **34**, 489 (1996).
16. The coherence of an interferogram measures the similarity of a pixel phase to the phase of its neighbors. When fringes in an interferogram can be visually discriminated, its coherence is good. Change in surface characteristics reduces coherence. When the same radar image exhibits low coherence whatever the image it is paired with, it generally means "climatic damage" to the radar image (such as that caused by snow cover).
17. M. A. Grant, I. G. Donaldson, P. F. Bixley, *Geothermal Reservoir Engineering* (Academic Press, New York, 1982).
18. The Mogi model was first applied to active volcanoes by K. Mogi [*Bull. Earthquake Res. Inst. Univ. Tokyo* **36**, 99 (1958)]. It was originally derived for a point source of pressure in an elastic half-space, but D. F. McTigue [*J. Geophys. Res.* **92**, 12931 (1987)] showed that it performs well for spherical sources of finite size, as long as $(a/d_{mogi})^5 \ll 1$, where a is the source radius. Surface subsidence is expressed as $h_{mogi}\, d_{mogi}^{\,3}\, (d_{mogi}^{\,2} + r^2)^{-3/2}$, where r is the horizontal distance from the source. Horizontal radial displacement is $h_{mogi}\, d_{mogi}^{\,2}\, r\, (d_{mogi}^{\,2} + r^2)^{-3/2}$.
19. If $v_{spreading}$ is parallel to the plate boundary, then Eq. 1 reduces to a model frequently used for strain accumulation across strike-slip faults [see, for example, J. C. Savage and R. O. Burford *J. Geophys. Res.* **78**, 832 (1973) and (*8*)].
20. We consider the source to represent the effect of material loss beneath d_{lock} because ductile extension there is not balanced by inflow of material from below. Surface subsidence caused by a line-source of pressure within an elastic half-space can be obtained by integration of the Mogi model (*18*). The model was first applied to Iceland rifts by E. Tryggvason [*J. Geophys. Res.* **73**, 7039 (1968)].
21. G. Bjornsson and B. Steingrimsson, *Temperature and Pressure in the Svartsengi Geothermal System* (Report 91016, National Energy Authority, Reykjavik, Iceland, 1991).
22. B. Brandsdottir, P. Einarsson, K. Arnason, H. Kristmannsdottir, *Refraction Measurements and Seismic Monitoring During an Injection Experiment at the Startsengi Geothermal Field in 1993* (Report RH-03-94, Science Institute, University of Iceland, Reykjavik, Iceland, 1994).

23. We thank two anonymous reviewers for comments, D. Massonnet for discussion and an early review of the manuscript, K. Feigl for discussion, and the European Commission for financial support for F.S. (grant PL95027). The General Mapping Tool public domain software was used to prepare figures.

16 August 1996; accepted 13 November 1996

Recalibrated Mariner 10 Color Mosaics: Implications for Mercurian Volcanism

Mark S. Robinson* and Paul G. Lucey

Recalibration of Mariner 10 color image data allows the identification of distinct color units on the mercurian surface. We analyze these data in terms of opaque mineral abundance, iron content, and soil maturity and find color units consistent with the presence of volcanic deposits on Mercury's surface. Additionally, materials associated with some impact craters have been excavated from a layer interpreted to be deficient in opaque minerals within the crust, possibly analogous to the lunar anorthosite crust. These observations suggest that Mercury has undergone complex differentiation like the other terrestrial planets and the Earth's moon.

One unresolved question from the Mariner 10 exploration of Mercury is whether widespread plains deposits formed due to volcanism or basin formation–related impact ejecta (*1–3*). We recalibrated and analyzed the Mariner 10 first encounter approach color data to address this fundamental issue. Previous analyses of Mariner 10 images defined color units on Mercury which indicated that color boundaries often did not correspond to photogeologic units, and no low albedo relatively blue mercurian materials were found that correspond to lunar mare deposits (*4, 5*). The calibration employed in these earlier studies did not completely remove vidicon blemishes and radiometric residuals. These artifacts were sufficiently severe that the authors presented an interpretive color unit map overlaid on monochromatic mosaics while publishing only a subset of the color ratio coverage of Mercury (*4–7*). We derived a refined calibration that increased the signal-to-noise ratio of these mercurian image data. These recalibrated image mosaics show the complete ultraviolet (UV) orange color data for this portion of Mercury. We interpret these recalibrated data in terms of the current paradigm of visible color reflectance for iron-bearing silicate regoliths (*5, 6, 8*).

The Mariner 10 vidicon imaging system was spatially nonuniform in bias and dark current, as well as being nonlinear at the extremes of the light transfer curve (*9*). Prelaunch flat field images acquired at varying exposure times allowed for the derivation of a nonlinearity and sensitivity nonuniformity correction, while an average of inflight images of deep space corrected for system offset (*10*). We utilized low-contrast Mariner 10 images of the venusian atmosphere to identify vidicon blemishes and create a stencil from which affected areas were simply deleted from all the mercurian images. Two spatially redundant mercurian mosaic sequences were processed for each filter and thus little areal coverage was lost due to the blemish deletion procedure. Instead of overlaying each image during the mosaicking, the images were averaged so that each pixel was formed from one to seven frames. The data were resampled to 3 km per pixel (original data were 2 to 3 km per pixel)

M. S. Robinson, United States Geological Survey, 2255 North Gemini Drive, Flagstaff, Arizona, 86001, USA.
P. G. Lucey, Hawaii Institute of Geophysics and Planetology, University of Hawaii, Honolulu, HI 96822, USA.

*To whom correspondence should be addressed. E-mail: robinson@flagmail.wr.usgs.gov